

Static Beam Shaping Using DMD And Its Application On Microscopy

Pan Zhang 10624939

(Dated: June, 2024)

In this project, we demonstrate that digital micromirror devices (DMDs) with a resolution of 1440×912 can manipulate both the amplitude and phase of the incoming beam by grouping each small micromirror into larger squares called superpixels. The superpixel methods achieve static wavefront shaping, and the fidelity of the target field is verified by off-axis holography. The mean square error (MSE) of the experiment beam intensity is bounded within 0.25, while the fidelity of the experiment beam phase diagram is bounded within 20%. This system can be incorporated into novel quantum microscopes to break diffraction limits and investigate quantum information.

I. INTRODUCTION

The spatial light modulators, including DMDs and liquid crystal devices, have found numerous applications since their invention. For instance, digital micromirror devices can perform tasks such as compressive sensing [1–3], hyperresolution microscopy [4, 5], terahedral imaging [6], and 3-dimensional imaging [7]. On the other hand, liquid crystal devices are adept at manipulating the polarization and phase of beams, making them more suitable for wavefront shaping applications [8].

Digital micromirror devices integrate millions of micromirrors, each the size of a micron, onto a complementary metal-oxide-semiconductor (CMOS) substrate. Each micromirror can individually tilt either -12 degrees or +12 degrees relative to the normal plane. Electrodes, springs, and torsion hinges are etched onto the CMOS substrate, and a CMOS memory circuit is created through lithography to synchronize the actions of the millions of micromirrors [9, 10]. This design enables the DMD to function as a fast spatial light modulator capable of reaching frequencies up to 400 MHz.

Liquid crystal devices, on the other hand, are constructed using special liquid crystal materials that exhibit properties of both liquids and solids. Like DMDs, liquid crystal modulators consist of millions of small pixels. However, these pixels are made of homogeneously oriented liquid crystal molecules. The orientation of these molecules can be manipulated by applying an electric field, which in turn determines the optical axis. This precise control over the orientation of liquid crystal molecules allows for precise manipulation of beam intensity, phase, and polarization. However, the lower refresh rate of liquid crystal devices (typically 60 Hz) compared to digital micromirror devices limits their application in certain scientific research contexts.

Phase manipulation is crucial in various fields such as holography [11], optical tweezers [12, 13], and wavefront shaping [14]. Many applications in these fields require a high refresh rate, prompting researchers to explore methods for phase control using DMDs. Considering that the time taken to reach the normal plane of a DMD differs as the incoming beam is projected at 24 degrees to the DMD's normal plane, while the reflected outgoing beam returns to the normal plane, phase manipulation

can be achieved by appropriately grouping small pixels into larger ones. At this stage, researchers have demonstrated that DMDs have full capabilities in controlling both the amplitude and phase of light [15, 16].

Traditional microscopes are constrained by Abbe diffraction limits. In recent decades, researchers have developed various methods to overcome these limits, including structured illumination microscopy [17–19], near-field scanning microscopy [20], and evanescent wave microscopy [21]. These methods either encode the image into the frequency domain for later recovery using computational methods or utilize the non-diffracting properties of near-field light, achieving resolutions at the nanometer scale.

Using DMDs, it is possible to shape light into non-diffracting patterns as a preprocessing step. Well-known examples include Bessel beams [22, 23], Airy beams [24], and lattice beams [25]. These beams can self-heal after passing through an turbid media such as biological tissue, significantly enhancing final resolution without the need for post-processing techniques. Hence, DMDs can make microscopy systems more compact, more scalable.

Furthermore, in recent years, researchers have shown that spatial light modulators (SLMs) can encode beams polarization as qubits [26], enabling direct reconstruction of the transverse light field wavefunction. This advancement has the potential to contribute to novel quantum microscopy techniques capable of directly measuring object wavefunctions.

In this project, our aim is to achieve static beam shaping by modulating both the phase and amplitude of the beam using DMD and optical devices. This compact system holds promise for advancing research in quantum information and high-resolution quantum microscopy.

II. METHODS

The DMD has a resolution of 1140×912 , meaning that there are 1140 and 912 micromirrors with dimensions of $7.6\mu m \times 7.6\mu m$ arranged in rows and columns respectively, forming individual pixels. The states of each pixel, independent of others, can be either on (tilted by 12 degrees) or off (tilted by -12 degrees).

The Ajile driver bridges the personal computer and

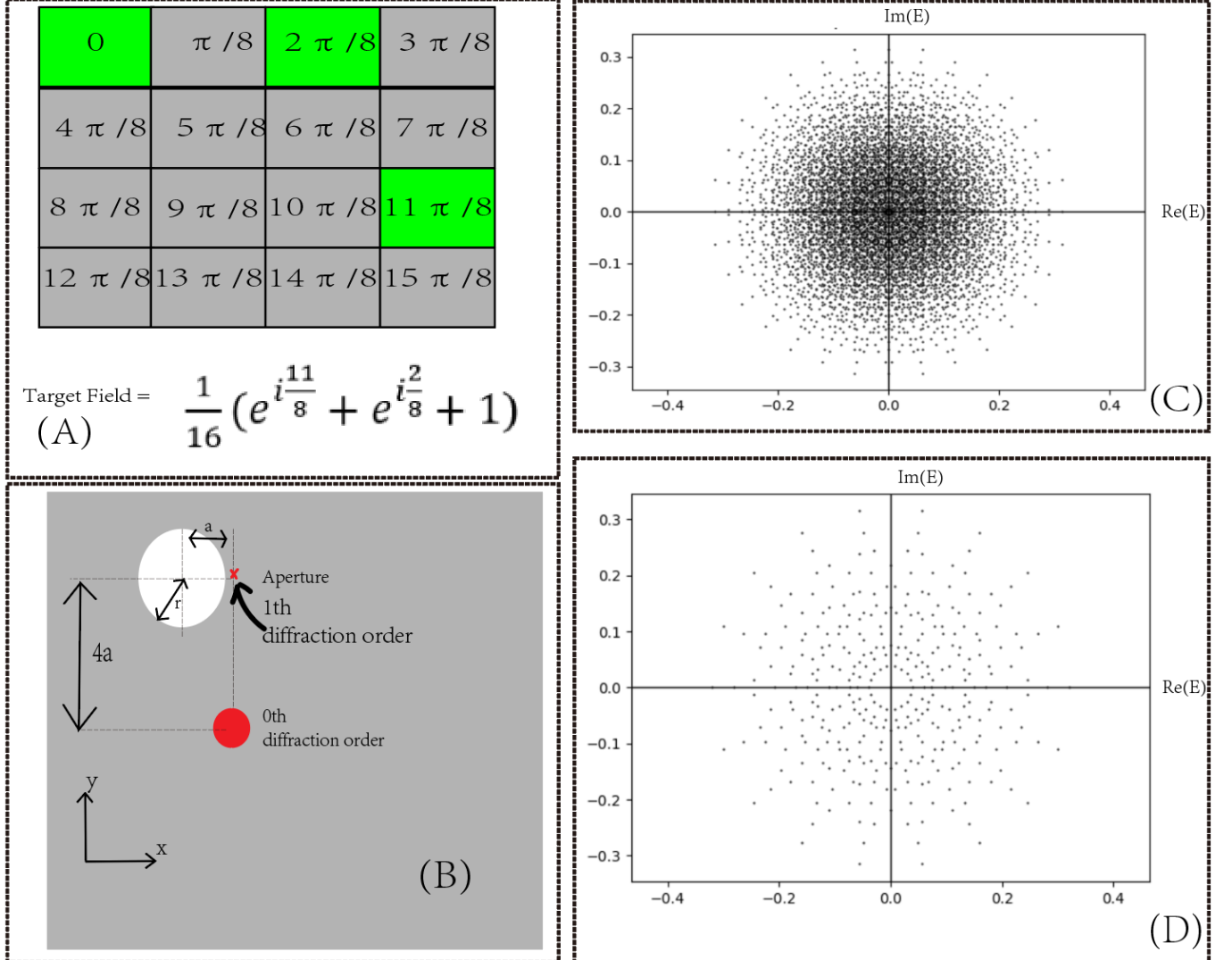


FIG. 1: The schematic depicts the principle of superpixel methods. In (A), small pixels are grouped into 4×4 arrays to form a superpixel. The spatial filters are placed around the first diffraction order in the Fourier plane, as shown in (B), such that the phase response of the small pixels in the target field is distributed uniformly from 0 to 2π . In (C) and (D), there are the complex fields of 4×4 superpixels and 2×2 superpixels, respectively, which can represent 343 different points and 6561 different points in the complex plane, respectively

the DMD. We send a 1140×912 matrix whose elements represent grayscale values ranging from 0 to 255 from the personal computer to the Ajile driver. A value of 0 represents a fully off state of a pixel, while 255 represents a fully on state. Intermediate values between 0 and 255 control the pixel's duration in the off and on states. The Ajile driver feeds the DMD with decoded matrix elements and synchronizes the motion of all pixels. This means that the pixels represent on and off states according to the corresponding matrix elements simultaneously after projection, and we define this action as one frame. Ten frames would require ten matrices input from the personal computer.

Each pixel can clearly reflect light and is only subject to amplitude manipulation. In this section, we want to

introduce the superpixel method [15], which endorses the DMD for both amplitude and phase modulation.

A. Superpixel Method

To control both the phase and intensity of the beam, we group the small pixels into superpixels, each comprising $n \times n$ small pixels. We employ the optical system depicted in Fig. 2 (A), consisting of a DMD, two plano-convex lenses, and a spatial filter (pinhole). The plano-convex lenses focus the reflected parallel beams from the DMD into the Fourier plane, where a low-pass spatial filter is positioned around the first diffraction orders (Fig. 1 (B)). This spatial filter introduces different light paths,

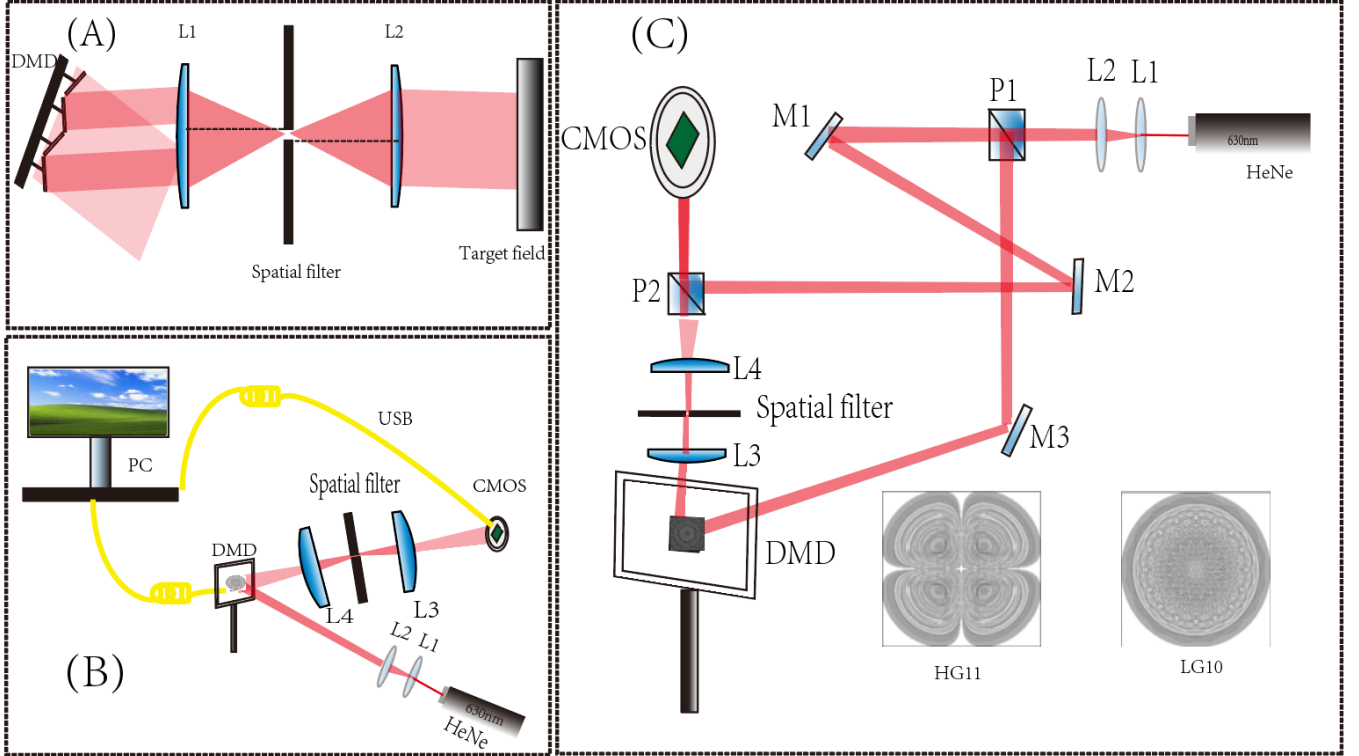


FIG. 2: The schematic depicts the layout of the experiment. In (a), the off-axis arrangement of optical devices achieves intensity and phase manipulation on the target field. In (b), the full illustration of optical systems used for static beam manipulation is provided. In (c), the off-axis holography experiment is conducted to verify the phase of the target field.

causing the phase response of small pixels to differ by $\frac{2\pi}{n^2}$ to adjacent horizontal pixels and by $\frac{2\pi}{n}$ to adjacent vertical pixels. For a superpixel of size $n \times n$, the phases of these smaller pixels are uniformly distributed from 0 to $2\pi(n^2-1)$. The intensity represented by a superpixel depends on its size and can have n^2 different levels, while different phase angles can be represented by activating different combinations of small pixels. For example, as illustrated in Fig. 1 (A), activating the first and third pixels on the first row and the fourth pixel in the third row results in a target field response represented by the summation of these three small pixels: $\frac{1}{16}(e^{i1\frac{11}{8}} + e^{i1\frac{3}{8}} + 1)$.

The total number of target fields on the complex plane that a superpixel can represent equals the combination of intensity fields multiplied by the combination of phase angles, divided by two. Computationally, it is straightforward to determine all the points on the complex plane that a superpixel can represent by computing the combination of phase angles of small pixels and then removing duplicates. For example, as shown in Fig. 1(C) and (D), a 3×3 superpixel can represent 343 different fields on the target plane, while a 4×4 superpixel can represent 6561 different fields. Naturally, as the size of the superpixel increases, the number of fields that can be represented by superpixels on the target plane also increases.

Determining the position and size of the spatial filter is crucial, and we outline the method in detail using Fig.

2(B). The position can be easily determined through the following steps:

Firstly, the laser beam is expanded and collimated using lenses L1 and L2, ensuring that the beam size when reaching the DMD covers all the micromirrors. The incident beams should make a 24-degree angle to the normal plane of the DMD. Collimation and expansion of the beam ensure that the incident beam's intensity is homogeneous, minimizing errors in the target field. The 24-degree incident angle is a consequence of the blazed grating, and the 0th diffraction order is centered with this incident angle.

Secondly, the beam is reflected by the DMD and collected by the first plano-convex lens. Diffraction gratings are written on the DMD, resulting in dense diffraction orders appearing on the Fourier plane. The first diffraction order would appear around $(x,y) = (0, na)$, where

$$a = \frac{-\lambda f}{n^2 d} \quad (1)$$

, with f being the focal length of the first plano-convex lens, λ being the wavelength of the beam, and d being the size of the micromirrors. We place the center of our spatial filter at $(x,y) = (0, na)$.

Finally, we fine-tune the position and size of the spatial filter. We move the spatial filter horizontally slightly to the left such that the left neighbor of the first diffraction

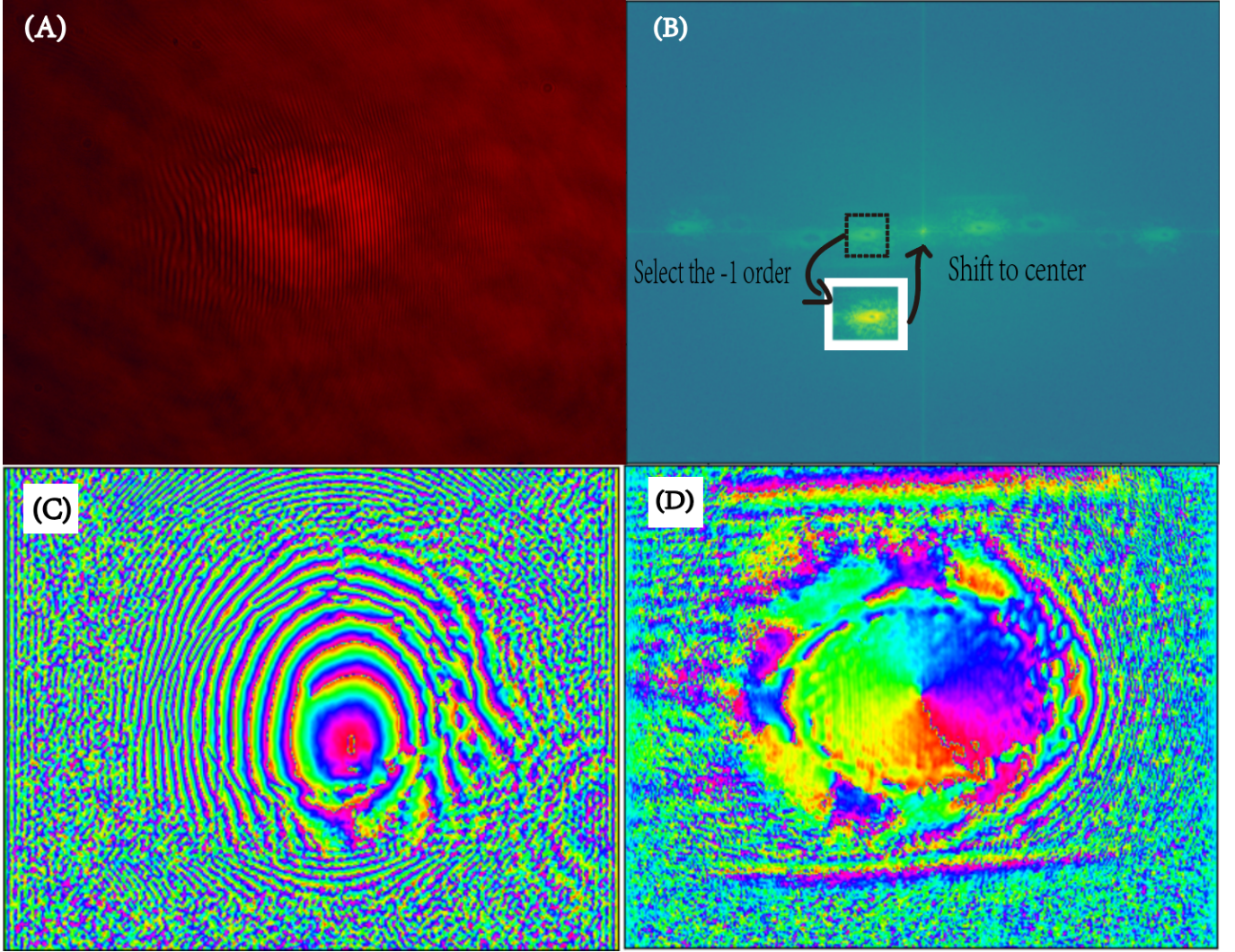


FIG. 3: The steps to reconstruct the phase diagram from holography are illustrated as follows: In (A), the raw LG10 mode holography image captured by a CMOS camera is shown. In (B), the -1^{st} order, 0^{th} order, and 1^{st} order are pronounced in the frequency domain, and only the -1^{st} order is selected and shifted to the center of the image. Subsequently, in (C), the phase diagram with background is reconstructed. After subtracting the background, the phase of LG10 can be accurately reconstructed.

order is located at the left edge of the spatial filter, and the first diffraction order is located at the right edge of the spatial filter.

The size of the spatial filter is adjusted to match the desired spatial bandwidth, given by

$$\Delta K = \frac{2\pi r}{\lambda f_1} \text{ rad pixel}^{-1} \quad (2)$$

. The desired spatial bandwidth is defined to be no higher than $\frac{\pi}{2n}$ rad pixel $^{-1}$. This size ensures that the spatial filter is small enough to blur the averaged light fields[27], making them spatially unresolvable so that the desired target field is shown on the target plane, and large enough to avoid disguising any expected field beam. The last plano-convex lens is used for collimation and beam amplification.

Slight displacement of spatial filters may slightly decrease the fidelity of the target field beam. For example, a 10% displacement of spatial filters would result in less than a 0.5% decrease in fidelity. In practical experiments, a 10% displacement of the spatial filter would cover part of the target field beam. Therefore, in general, as long as the intensity pattern on the target field resembles the expected field, the phase won't differ significantly, resulting in high fidelity of the target field.

B. Holography

To verify the phase and intensity modulation of superpixel methods, we utilize off-axis holography methods to reconstruct the phase diagram and intensity distribution

[28].

As shown in Fig. 2 (C), the HeNe laser beam is expanded after passing through the expanding lens group. Subsequently, the incident beams are split into two equal intensity beams by a beam splitter. One of the subbeams, denoted as E_s , directs to the DMD. The DMD projects different superpixel patterns, shaping the beam statically. The target field falls on the second beam splitter and recombines with the reference beam E_0 . The coherence length of the HeNe laser is around 30 cm. Two mirrors, M1 and M2, control the time of flight of the reference beams. Within the coherent length, the recombined beams show pronounced interference. This hologram is recorded by a CMOS camera. The recombined beam field can be described by the equation:

$$I = |E_0|^2 + |E_s(x, y)|^2 + E_0 E_s^*(x, y) e^{ik \sin(\theta x)} + E_0^* E_s(x, y) e^{-ik \sin(\theta x)} \quad (3)$$

, where E_0 is the reference beam wavefunction, E_s is the target field wavefunction, θ is the relative angle between reference beam and target field exiting the second beam splitter, k is the wavevector.

The Fourier transform of the hologram gives a symmetrically distributed pattern in the frequency domain. The zeroth order $|E_0|^2 + |E_s(x, y)|^2$ is centralized and contains the information of the wavefunction amplitude distribution. The -1 order $E_0^* E_s(x, y) e^{-ik \sin(\theta x)}$ is directly proportional to the phase of object wavefunction. We manually select (fig) the -1 order on the frequency domain and perform an inverse Fourier transform back into the intensity domain. This yields the phase diagram.

As an example, we present the Gaussian Laguerre 10 mode phase diagram reconstruction in Fig. 3. We use the DMD to create a superpixel pattern corresponding to the LG10 mode. The recorded holography is presented in Fig. 3 (A). We perform the two-dimensional Fourier transform with respect to the hologram, and three orders are shown in the frequency domain in Fig. 3 (B). We shift the -1 order, which is in the dashed line square, to the center of the frequency domain. The inverse Fourier transform gives the phase diagram in Fig. 3 (C). After removing the background, the phase diagram of the LG10 mode in Fig. 3 (D) is precisely reconstructed with an error bound of 15%.

C. High order Gaussian Beams

In our experiment, we aim to shape a Gaussian beam into non-diffracting beams to advance microscopy resolution to the hundred nanometer scale. Motivated by this goal, we investigate several well-known and well-studied beams, including Gaussian Laguerre beams (LG mode), Gaussian Hermite modes (HG mode), and non-diffracting Bessel modes (B mode).

The HG mode is described by the complex function[29]:

$$E(x, y, z) = \frac{1}{N} H_m \left(\sqrt{2} \frac{x}{w(z)} \right) H_n \left(\sqrt{2} \frac{y}{w(z)} \right) \times \exp \left(-\frac{x^2 + y^2}{w(z)^2} \right) \times \exp \left(-ik \frac{x^2 + y^2}{2R} + ikz - i(n+m+1) \arctan \left(\frac{z}{kw_0^2/2} \right) \right) \quad (4)$$

, where H represents the Hermite polynomial, w is the beam radius after displacement z from the beam waist, R is the radius curvature of the wavefront, n and m are different Hermite mode numbers, w_0 is the beam waist, and x and y are transverse displacements.

The LG mode is described by the complex function[29, 30]:

$$E(x, y, z) = \frac{1}{N} \left(\frac{w_0}{w(z)} \right)^l \left(\sqrt{2} \frac{r}{w(z)} \right)^l \exp \left(-\frac{r^2}{w(z)^2} \right) \times Lp^{|l|} \left(\frac{2r^2}{w(z)^2} \right) \exp \left(-ik \frac{r^2}{2R} - il \arctan \left(\frac{y}{x} \right) \right) + i(l+2p+1) \arctan \left(\frac{z}{kw_0^2/2} \right) \quad (5)$$

, where l and p are azimuthal and radial indices respectively, Lp is the Laguerre function.

Finally, the non-diffracting Bessel mode is described by the equation[31]:

$$E(x, y, z) = \exp(ikz) \cdot J_m(kr) \cdot \exp(im \cdot \arctan(\frac{y}{x})) \quad (6)$$

, where m is the mode of the Bessel beam, and J_m is the Bessel function. Understanding the complex functions of these beams enables us to shape the transverse beam field using the superpixel method. The shaped beams, depending on the quality of optical and laser devices, present high-quality static beam shaping. Importantly, the light evolves as it propagates along the z-axis, similar to using other methods to generate these beams.

The DMD we utilized in the experiment has a resolution of 912×1140 . By using 4×4 size superpixels, a total resolution of 228×285 for the target field can be achieved. Spatial filters are positioned around (x, y) , and the iris size is restricted to be no more than the specified size. This forms a 228×285 complex phase matrix. We developed a Python program to efficiently convert this complex phase matrix into a binary matrix readable by the DMD. Therefore, using our program, LG, HG, or any other time-independent transverse light field can be projected onto the target field.

To project a time-dependent transverse light field, we could discretize the transverse wavefunction profile into

small time steps. However, the refresh rate of the DMD may not be sensitive enough to accurately represent the fast-evolving wavefield.

III. DISCUSSION

A. Experiment details

To test both the intensity and phase of the target field, we designed our experimental system as depicted in Fig. 2 (C). The expanding lens group L1 and L2 have focal lengths of $f_1 = 350\text{mm}$ and $f_2 = 500\text{mm}$, respectively. The incident laser beam to the first lens can be approximated as parallel light. Therefore, placing the separation between L1 and L2 at 850mm results in a beam magnification of $M = \frac{f_2}{f_1} = 1.43$.

The beam then passes through the polarized beam splitter P1 (Thorlab PBS201, 20mm \times 20mm) and is split into two beams. The reference beam is directed into the second polarized beam splitter and recombined with the object beams. The object beams incident on the DMD at a 24-degree angle, which centralizes the 0th diffraction order on the Fourier plane.

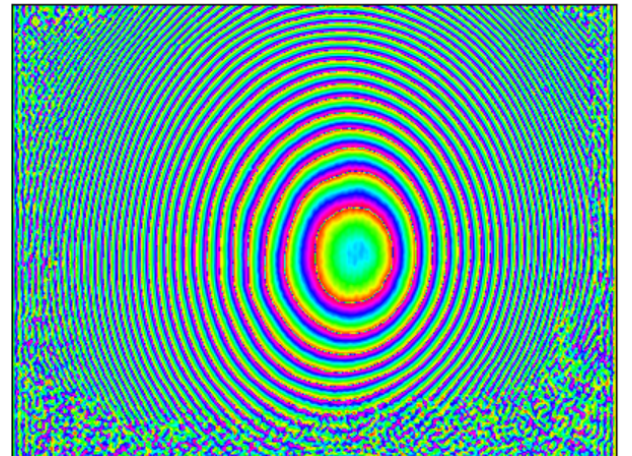
Lenses L3 and L4 are two plano-convex lenses with one side surface having no curvature. Their focal lengths are $f_3 = 100\text{mm}$ and $f_4 = 75\text{mm}$, respectively. Using Equation 1, we compute the position of the spatial filter $(x, y) = (-a, na) = (-0.5, 3.4)\text{mm}$ relative to the 0th order diffraction, where $a = \frac{633\text{nm} \times 100\text{mm}}{4^2 \times 7.6\mu\text{m}} = 0.52\text{mm}$. The radius of the spatial filter, calculated using Equation 2, is set to be 0.52mm.

The polarizations introduced by P1 and P2 effectively cancel each other out, having no effect on the target field wavefunction. To measure the intensity profile of the target field, we simply block the reference beams. We unblock the reference beam to create a hologram.

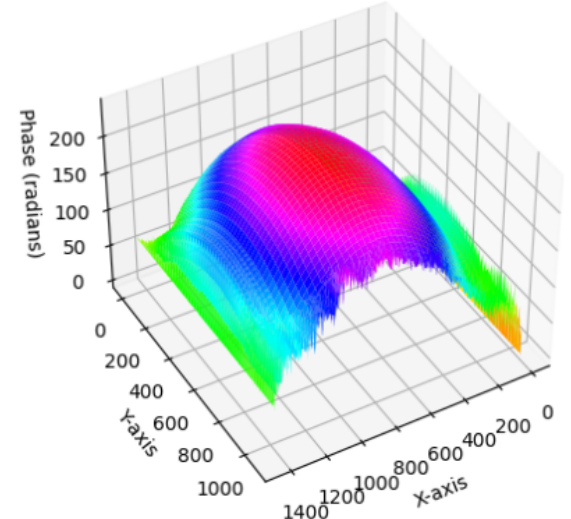
The wavefront of the light source is a multimode Gaussian beam. We utilize the DMD to shape the Gaussian beam into LG, HG, and B modes using Equations 2 and 3 respectively. We set the beam waist, w_0 , to be 1mm and assume the beam propagates along the z-axis for 1mm. Consequently, the beams shaped by the DMD act as if they have a 1mm beam waist and have already propagated for 1mm in longitudinal direction.

We meticulously recorded the intensity and hologram of various types of beams, including HG_{00} , HG_{10} , HG_{11} , HG_{21} , LG_{10} , LG_{11} , LG_{21} , B_0 , B_1 , B_2 , and B_3 beams, using the Thorlabs CMOS camera (1.6 MP CMOS Compact Scientific Cameras). In addition to recording these beams, it is crucial to generate a plane wave using the DMD and record its hologram. Since the hologram of the plane wave beam encodes information about noise and does not involve additional phase, we can utilize its reconstructed phase diagram to remove noise in the phase reconstruction of beams.

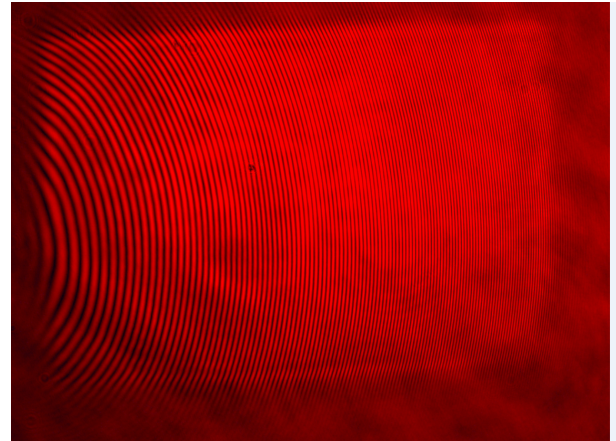
To generate a plane wave, the superpixels are set to equal points on the complex plane. We choose e^0 as this



(a) The phase diagram of plane wave.



(b) Unwrapped phase diagram.



(c) The hologram of planewave.

FIG. 4: The planewave hologram is shown in (C). From (a), the wavefront of HeNe laser is clear and using np.unwrap a clear wavefront is presented in (b).

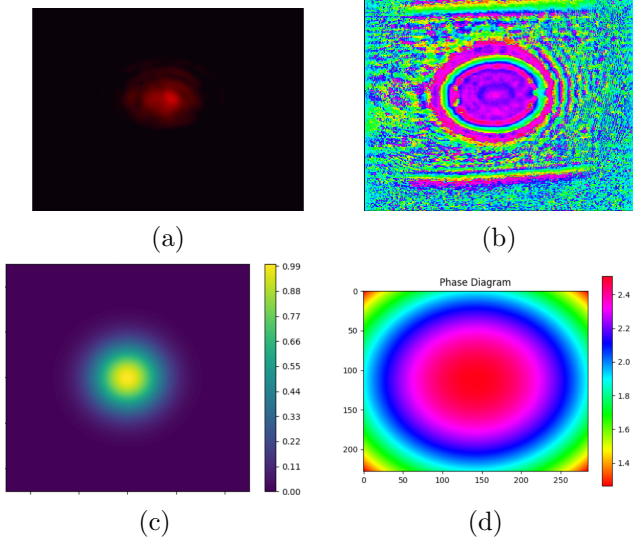


FIG. 5: The experiment intensity and phase profile of HG00 beam in (a) and (b). The predicted intensity and phase profile of HG00 beam in (c) and (d)

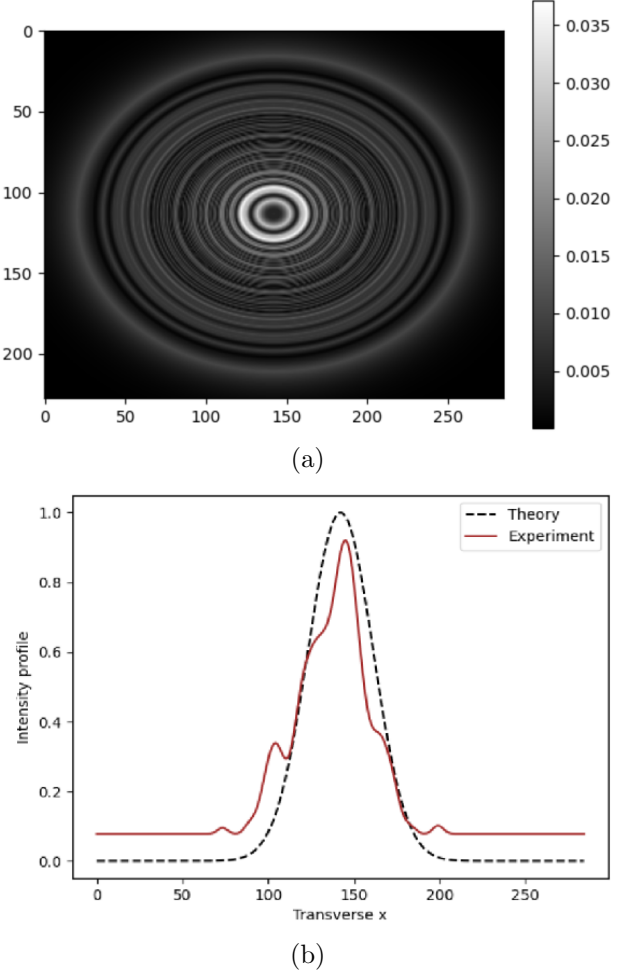


FIG. 6: The error map in (a) and the compare the theory and experiment HG00 intensity profile in (b). The error from DMD pattern is 0.52%.

point, as it allows for the highest intensity in the hologram. Turning on all eight mirrors in the upper two rows corresponds to generating this plane wave and minimizes intense diffraction. The hologram of the plane wave and its phase reconstruction are depicted in Fig. 4.

Analysis of the hologram of the plane wave reveals that the reference beam is set off-axis, evidenced by the curved interference fringes bending toward the left and the center of the fringes, corresponding to the central axial of the light source wavefront, significantly shifting out of the left boundary of the image. This off-axis configuration of the hologram helps prevent overlap between orders in the Fourier frequency domain. Furthermore, besides the wavefront from the HeNe laser, we observe several other wavefronts in the hologram originating from internal reflections of lenses lacking coatings to prevent internal reflections.

In Fig. 4(a), the phase diagram resembling concentric rings elucidates the HeNe wavefronts. We employ a phase unwrapping algorithm to obtain continuous phase values from periodic phase values, as demonstrated in Fig. 4(b).

Obtaining the phase diagram of the plane wave provides the best reference for removing noise from the phase diagrams of LG, HG, and B mode beams. The phase diagrams of beams modes after subtracting the background are presented in Fig. 5 and Appendix Fig.9. Then intensity profile are directly imaged by CMOS camera when blocking the reference beams and are shown in Appendix Fig.8.

B. Fidelity and Error Analysis

The amplitude and phase diagrams on the target plane closely resemble the simulation, as evidenced by the experimental results of HG00 in Fig. 5a and Fig. 5b, along with the predicted intensity and phase profiles in Fig. 5c and Fig. 5d. To further investigate the sources of errors, we delve into the fidelity of the transverse amplitude and phase profiles.

To verify the intensity fidelity, we compute the Mean Squared Error (MSE) of the intensity profile. Initially, we convert the image into a two-dimensional matrix using the cv2 library. Each matrix element ranges from 0 to 255, representing the grayscale range. We normalize the matrix by dividing all elements by 255, rescaling it from 0 to 1. Subsequently, we extract a row of experimental data from the 2D matrix and compare it with a row of the theoretically predicted intensity profile. The mean square error is computed using the formula: $MSE_i = \frac{1}{n} \sum_{i=1}^n (A_i - B_i)^2$. We then compute the total MSE: $MSE = \sum_{i=1}^n MSE_i$. An example of the cross-section of HG00 is presented in Fig. 6(b) and Appendix Fig. 11. We compute the MSE of the intensity profile for all beams, summarized in Fig. 7 (A).

The fidelity of the phase of each beam mode is further investigated using histograms(Fig. 12, Fig. 13). We observe that the phase diagrams exhibit a global phase

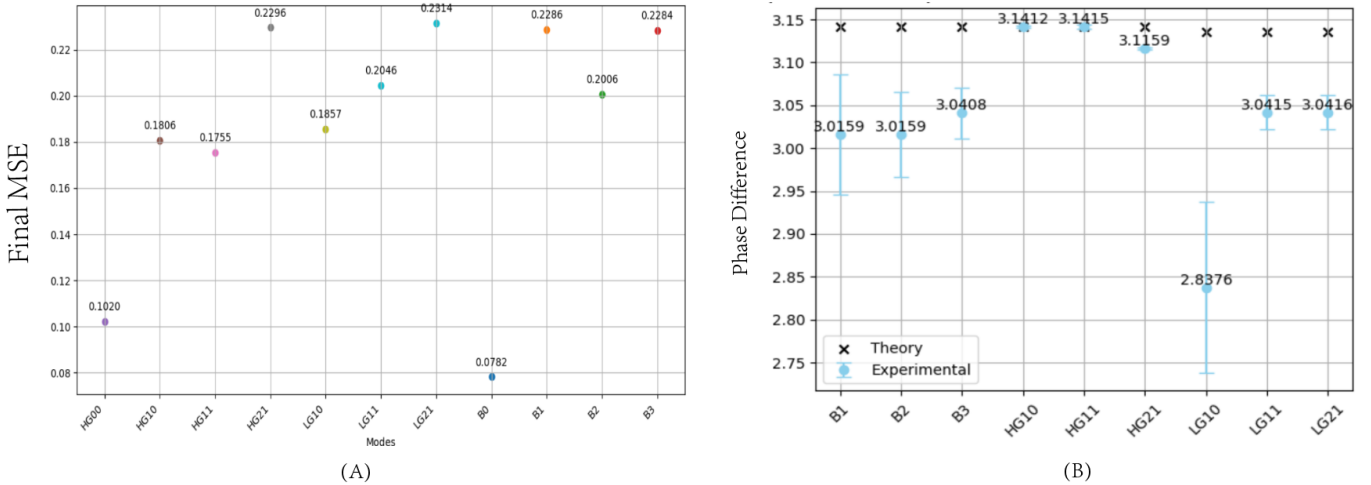


FIG. 7: Summary of MSE for all different beam modes in (A). The summary of phase difference between two peaks of histogram in (B).

difference and periodicity (Fig. 9, 10), rendering the computation of MSE inaccurate. Upon observing the B mode and LG mode wavefunctions, we realize that the phase value along the edge of a circle should be periodic. This implies that when we statistically analyze the phase values into a histogram, there must exist two peaks and two troughs. The phase difference between these peaks or troughs endows the properties of the phase information and can be utilized to compute the phase fidelity.

The HG mode behaves slightly differently, as shown in the Appendix Fig.9. The phase of the HG mode (Fig. 9d, 9e, 9f, 9g) appears to be quite binary, resembling a delta function-like histogram (Fig. 12d, 12e, 12f, 12g). The histogram from the experimental phase diagram thus presents a Lorentzian shape, with the bandwidth illustrating the propagated errors, including inaccuracies in placing the spatial filters, errors in Fourier transformation, and interference from multimode laser sources, among others. The summary of phase difference between two peaks of phase is presented in Fig. 7 (B).

We conducted five different groups of experiments on beams of five slightly different in sizes to analyze the errors of the Mean Squared Error (MSE) and phase difference. Surprisingly, the error bar for MSE is too small to discern, while the errors for the phase difference are significant. This discrepancy arises because the MSE is suppressed by large blank areas containing small signal values, resulting in a large denominator, while the squared errors in the numerator are small. For LG and B mode phase diagrams, there are no small signal values to reduce the error, and all signals exhibit no significant differences. A small perturbation in the phase diagram would thus introduce a pronounced error. This is not the case for the HG mode, where the Lorentzian-shaped histogram has many small signal values, making the peaks clear.

The errors in intensity mainly stem from unfavorable

experimental conditions. The HeNe laser we utilized is not a single-mode laser, resulting in low spatial and spectral purity, high divergence, and low coherence. As depicted in the Fig.8 and Fig.9, numerous speckles are visible in both the spectral and phase fields, primarily caused by the self-interference of the multimode laser beam. Other potential factors, such as optical defects, fingerprints, and dust on optical devices, have been meticulously avoided. Furthermore, the Class 3R laser has a power of only 3mW. The superpixel method, which requires selecting only the 1st order diffraction, significantly deteriorates the intensity of the target field. Consequently, some intensity profiles exhibit non-uniform distributions.

Another main source of error is the conversion of complex functions into DMD patterns. As a reminder, we represent the continuous wavefunction as a two-dimensional discretized array. Subsequently, we compute the pixel combinations that represent the points on the complex plane that best match the corresponding matrix elements. Both of these steps introduce errors. To mitigate steep variations in the wavefunction and reduce discretization, we should compute the wavefunction near the beam waist, as the wavefront around the beam waist has a flatter curvature.

The error from converting the wavefunction matrix into DMD patterns is intrinsic. Fortunately, using 4×4 size superpixels, the error is well bounded within 1%. For instance, when converting the HG00 mode from a 2D matrix into a DMD pattern, the error map is illustrated in Fig. 6a. The combination of superpixels grows exponentially with the superpixel size, so the error is heavily suppressed. Hence, to further reduce the conversion error, we can use larger size superpixels, such as 8×8 , which reduce the error to less than $10^{-7}\%$.

Additionally, the optical devices introduce errors. We opted for a CMOS camera instead of a CCD camera,

which has a low dynamic range and high noise rate. While increasing the exposure time could potentially mitigate speckles with a CCD camera, this is not feasible with a CMOS camera as it quickly saturates the dynamic range. Moreover, the non-coating lenses induce internal reflections, generating several additional divergent beams. This can be observed in the phase diagram in Figure 3, where instead of the expected single spherical divergent beam from the HeNe laser, three wavefronts are present.

Despite the significant errors introduced by the suboptimal experimental setup, the relatively low MSE values and well-bounded phase errors indicate the success of the superpixel method.

IV. CONCLUSION AND FURTHERWORK

In conclusion, we have demonstrated the efficacy of the DMD in statically shaping beams using superpixel methods. By providing complex functions for Hermite-Gaussian beams, Laguerre-Gaussian beams, and non-diffracting Bessel beams, we successfully computed their transverse profiles and converted them into DMD patterns. The analysis of HG, LG, and B mode beams using off-axis holography methods revealed bounded errors, showcasing the precision of superpixel methods in static beam control.

However, drawbacks of the superpixel system, such as significant intensity loss due to the spatial filter and intrinsic errors in pattern conversion, are evident. Fortunately, these issues can be addressed by employing high-power lasers to compensate for intensity loss and using higher-resolution superpixels, such as 8×8 , to minimize conversion errors.

While generating specific beams requires specific optical arrangements, the scalability of the system is enhanced by the simplicity of beam shaping through DMD pattern changes. Moreover, beam size control is achievable by computing the beam at different positions relative to the beam waist.

Recent research on strong measurements of quantum wavefunctions using SLMs opens up intriguing possibilities. By encoding information into polarization qubits, strong measurement of transverse quantum wavefunctions can be achieved. The capability of DMDs to fully control beam amplitude, phase, and polarization, particularly when combined with superpixel methods, holds promise for various applications including optical tweezer systems, thin light sheet microscopy, quantum strong measurement systems, and more.

In summary, the DMD offers a versatile and affordable solution for precise beam control, with its high refreshing rate, low error rate, scalability, and robustness making it suitable for a wide range of applications. Further exploration and integration of this technology into diverse optical systems are warranted to unlock its full potential

-
- [1] M. F. Duarte, M. A. Davenport, D. Takhar, J. N. Laska, T. Sun, K. F. Kelly, and R. G. Baraniuk, Single-pixel imaging via compressive sampling, *IEEE Signal Processing Magazine* **25**, 83 (2008).
 - [2] E. Candès and J. Romberg, Sparsity and incoherence in compressive sampling, *Inverse Problems* **23**, 969–985 (2007).
 - [3] E. J. Candes and T. Tao, Near-optimal signal recovery from random projections: Universal encoding strategies?, *IEEE Transactions on Information Theory* **52**, 5406–5425 (2006).
 - [4] M. Dahan, Compressive fluorescence microscopy for biological and hyperspectral imaging, *Imaging and Applied Optics Technical Papers* 10.1364/isa.2012.im4c.5 (2012).
 - [5] C. Tao, H. Zhu, X. Wang, S. Zheng, Q. Xie, C. Wang, R. Wu, and Z. Zheng, Compressive single-pixel hyperspectral imaging using rgb sensors, *Opt. Express* **29**, 11207 (2021).
 - [6] J. Le, Y. Su, C. Tian, A. H. Kung, and Y. R. Shen, A novel scheme for ultrashort terahertz pulse generation over a gapless wide spectral range: Raman-resonance-enhanced four-wave mixing, *Light: Science amp; Applications* **12**, 10.1038/s41377-023-01071-z (2023).
 - [7] M.-J. Sun, M. P. Edgar, G. M. Gibson, B. Sun, N. Radwell, R. Lamb, and M. J. Padgett, Single-pixel three-dimensional imaging with time-based depth resolution, *Nature Communications* **7**, 10.1038/ncomms12010 (2016).
 - [8] Z. Yu, H. Li, T. Zhong, J.-H. Park, S. Cheng, C. M. Woo, Q. Zhao, J. Yao, Y. Zhou, X. Huang, and et al., Wavefront shaping: A versatile tool to conquer multiple scattering in multidisciplinary fields, *The Innovation* **3**, 100292 (2022).
 - [9] I. TEXAS, Dlp4500 (2022).
 - [10] D. Dudley, W. M. Duncan, and J. Slaughter, Emerging digital micromirror device (dmd) applications, *MOEMS Display and Imaging Systems* 10.1117/12.480761 (2003).
 - [11] R. S. Nesbitt, S. L. Smith, R. A. Molnar, and S. A. Benton, *SPIE Proceedings* 10.1117/12.343767 (1999).
 - [12] D. Stuart and A. Kuhn, Single-atom trapping and transport in dmd-controlled optical tweezers, *New Journal of Physics* **20**, 023013 (2018).
 - [13] G. Gauthier, I. Lenton, N. McKay Parry, M. Baker, M. J. Davis, H. Rubinsztein-Dunlop, and T. W. Neely, Direct imaging of a digital-micromirror device for configurable microscopic optical potentials, *Optica* **3**, 1136 (2016).
 - [14] A. B. Ayoub and D. Psaltis, High speed, complex wavefront shaping using the digital micro-mirror device, *Scientific Reports* **11**, 10.1038/s41598-021-98430-w (2021).
 - [15] S. A. Goorden, J. Bertolotti, and A. P. Mosk, Superpixel-based spatial amplitude and phase modulation using a digital micromirror device, *Optics Express* **22**, 17999 (2014).
 - [16] J. Aulbach, B. Gjonaj, P. M. Johnson, A. P. Mosk, and A. Lagendijk, Control of light transmission through opaque scattering media in space and time, *Physi-*

- cal Review Letters **106**, 10.1103/physrevlett.106.103901 (2011).
- [17] DMD-based LED-illumination super-resolution and optical sectioning microscopy, volume=3, doi=10.1038/srep01116, number=1, journal=Scientific Reports, author=Dan, Dan and Lei, Ming and Yao, Baoli and Wang, Wen and Winterhalder, Martin and Zumbusch, Andreas and Qi, Yujiao and Xia, Liang and Yan, Shaohui and Yang, Yanlong and et al., year=2013, month=Jan, .
- [18] J. D. Manton, Answering some questions about structured illumination microscopy, Philosophical Transactions of the Royal Society A: Mathematical, Physical and Engineering Sciences **380**, 10.1098/rsta.2021.0109 (2022).
- [19] Y. Gruenbaum, Faculty opinions recommendation of sub-diffraction multicolor imaging of the nuclear periphery with 3d structured illumination microscopy., Faculty Opinions – Post-Publication Peer Review of the Biomedical Literature 10.3410/f.1116332.572347 (2008).
- [20] B. Hecht, B. Sick, U. P. Wild, V. Deckert, R. Zenobi, O. J. Martin, and D. W. Pohl, Scanning near-field optical microscopy with aperture probes: Fundamentals and applications, The Journal of Chemical Physics **112**, 7761–7774 (2000).
- [21] M. Oheim, D. Loerke, R. H. Chow, and W. Stühmer, Evanescent-wave microscopy: A new tool to gain insight into the control of transmitter release, Philosophical Transactions of the Royal Society of London. Series B: Biological Sciences **354**, 307–318 (1999).
- [22] T. A. Planchon, L. Gao, D. E. Milkie, M. W. Davidson, J. A. Galbraith, C. G. Galbraith, and E. Betzig, Rapid three-dimensional isotropic imaging of living cells using bessel beam plane illumination, Nature Methods **8**, 417–423 (2011).
- [23] S. Takanezawa, T. Saitou, and T. Imamura, Wide field light-sheet microscopy with lens-axicon controlled two-photon bessel beam illumination, Nature Communications **12**, 10.1038/s41467-021-23249-y (2021).
- [24] C. Liu, Y.-L. Liu, and T. Yeh, Light-sheet microscopy using attenuation-compensating airy beam, Biophysical Journal **112**, 10.1016/j.bpj.2016.11.796 (2017).
- [25] A. Yap, Faculty opinions recommendation of lattice light-sheet microscopy: Imaging molecules to embryos at high spatiotemporal resolution., Faculty Opinions – Post-Publication Peer Review of the Biomedical Literature 10.3410/f.723891050.793507811 (2015).
- [26] Compressive direct measurement of the quantum wave function, volume=113, doi=10.1103/physrevlett.113.090402, number=9, journal=Physical Review Letters, author=Mirhosseini, Mohammad and Magaña-Loaiza, Omar S. and Hashemi Rafsanjani, Seyed Mohammad and Boyd, Robert W., year=2014, month=Aug, .
- [27] E. G. van Putten, I. M. Vellekoop, and A. P. Mosk, Spatial amplitude and phase modulation using commercial twisted nematic lcds, Applied Optics **47**, 2076 (2008).
- [28] E. Cuche, P. Marquet, and C. Depeursinge, Spatial filtering for zero-order and twin-image elimination in digital off-axis holography, Applied Optics **39**, 4070 (2000).
- [29] E. G. Abramochkin, V. V. Kotlyar, A. A. Kovalev, and S. S. Stafeev, Generalized asymmetric hermite-gaussian and laguerre-gaussian beams, Photonics **10**, 606 (2023).
- [30] Q. Zhan, Cylindrical vector beams: From mathematical concepts to applications, Advances in Optics and Photonics **1**, 1 (2009).
- [31] D. McGloin and K. Dholakia, Bessel beams: Diffraction in a new light, Contemporary Physics **46**, 15–28 (2005).

V. APPENDIX

In this section, we present the experimental outcomes of beam shaping comprehensively and compare them with the predicted high-order Gaussian beams, including Bessel Beams (B), Laguerre-Gaussian Beams (LG), and Hermite-Gaussian Beams (HG).

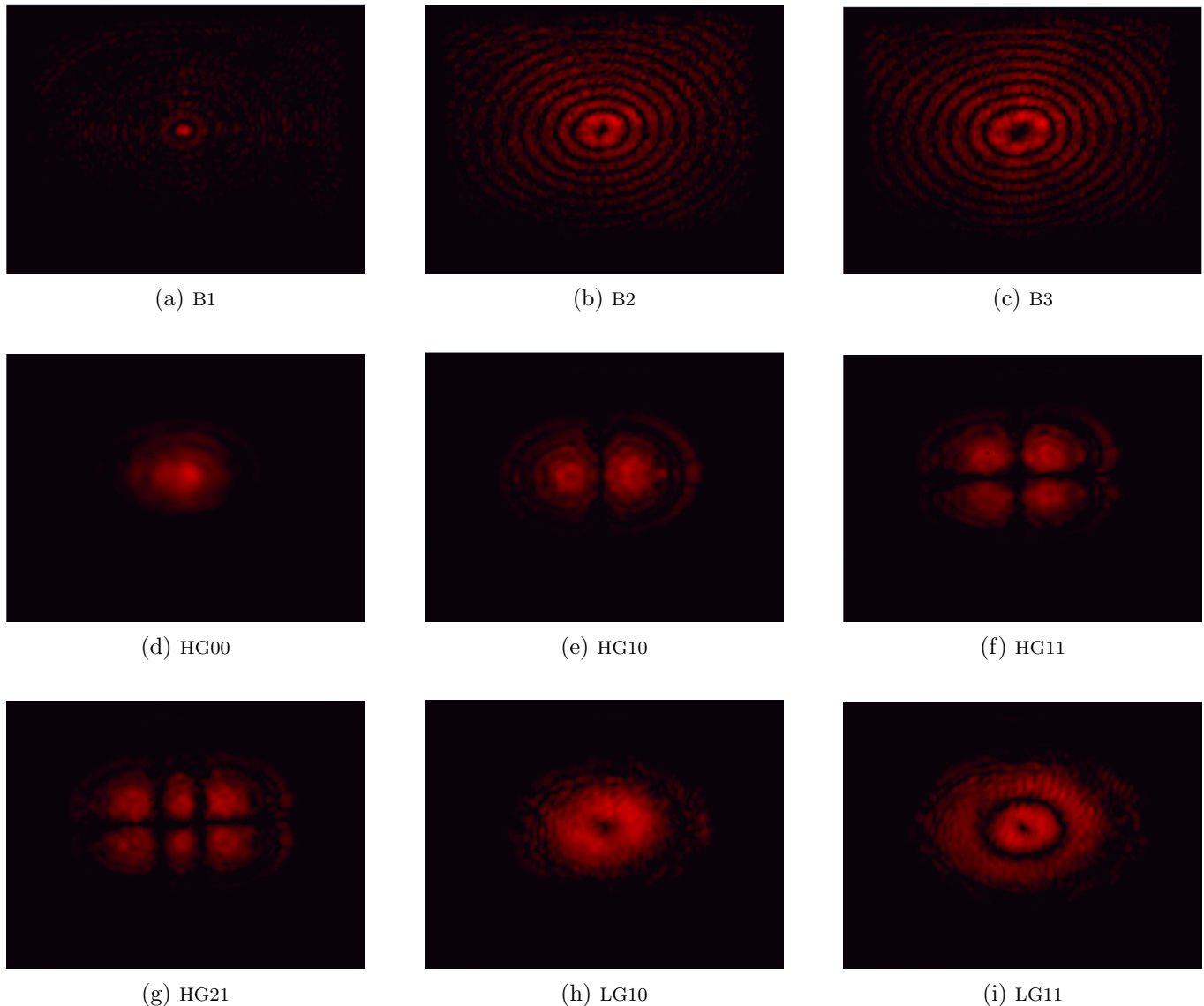


FIG. 8: High Order Gaussian Beams

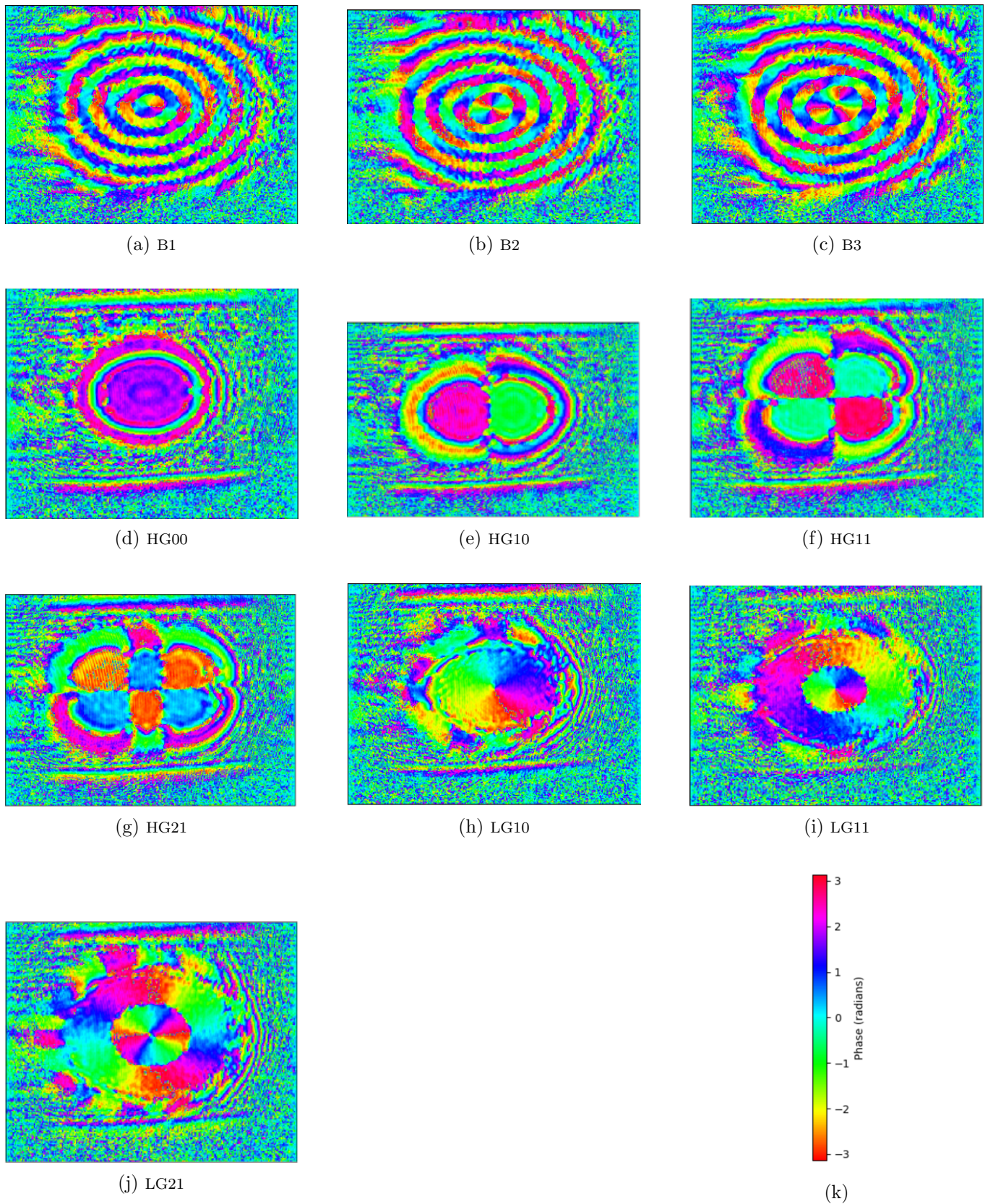


FIG. 9: High order Gaussian Beams phase diagram.

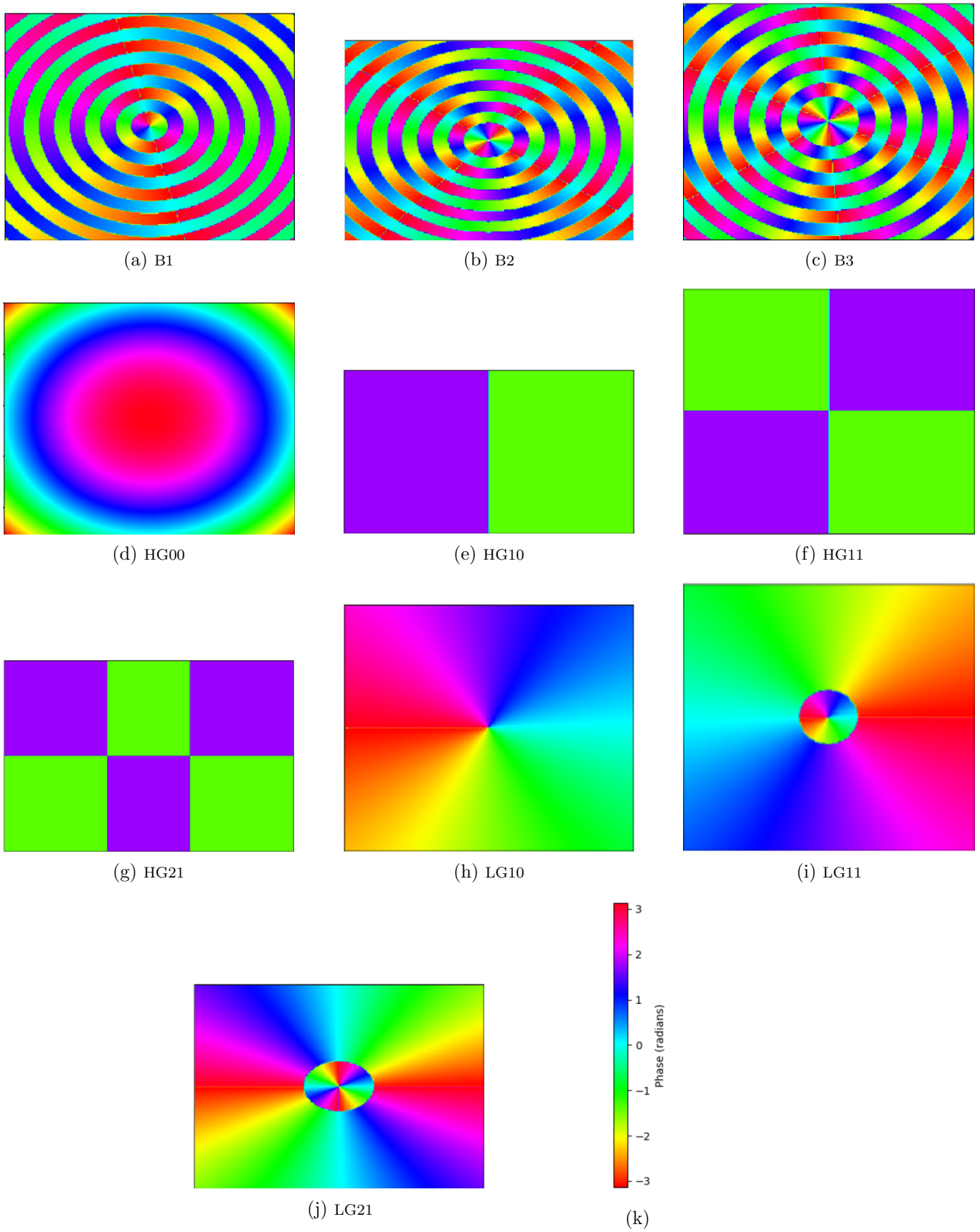


FIG. 10: Predicted Phase diagram

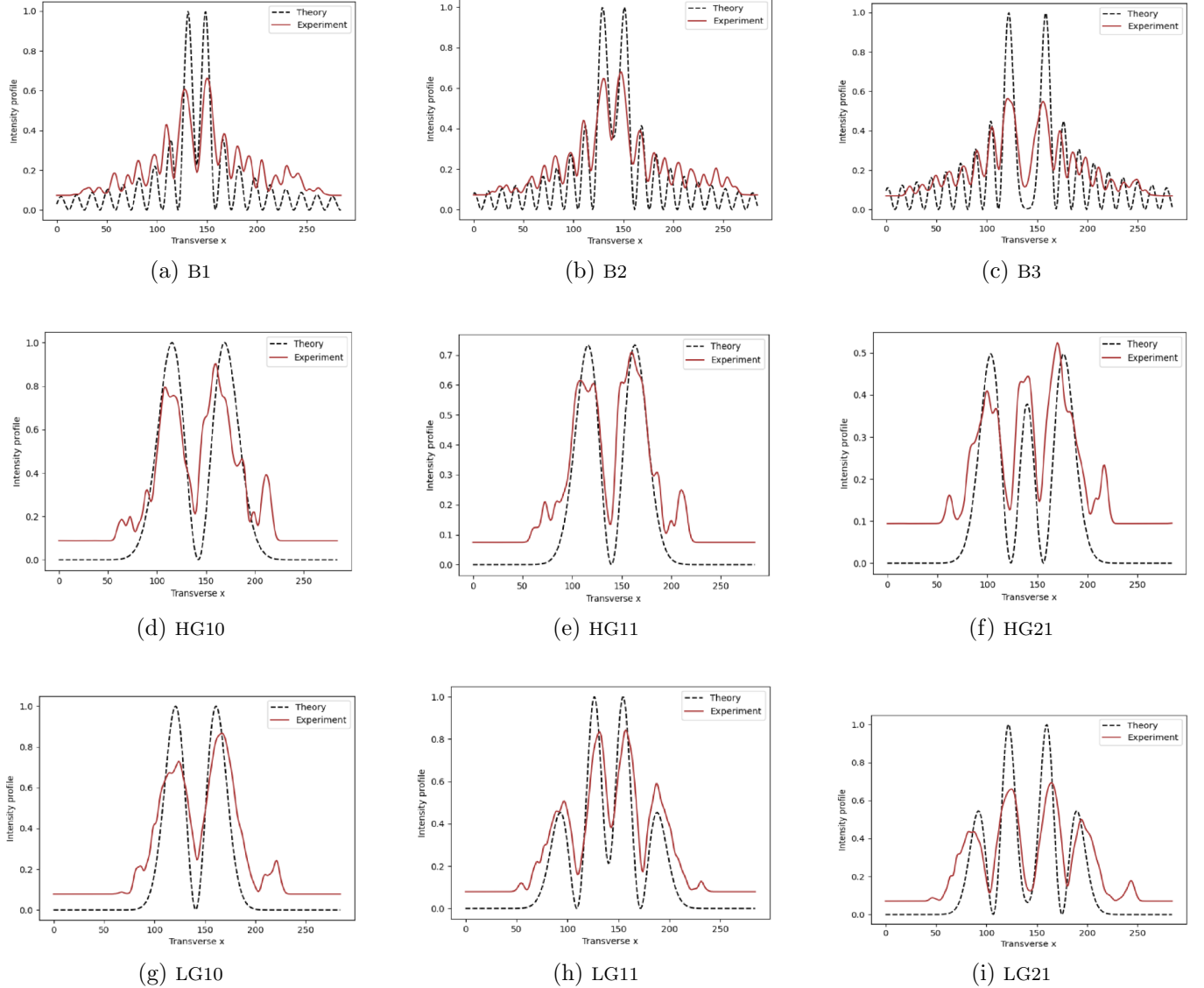


FIG. 11: Comparing theory and experiment intensity profile.

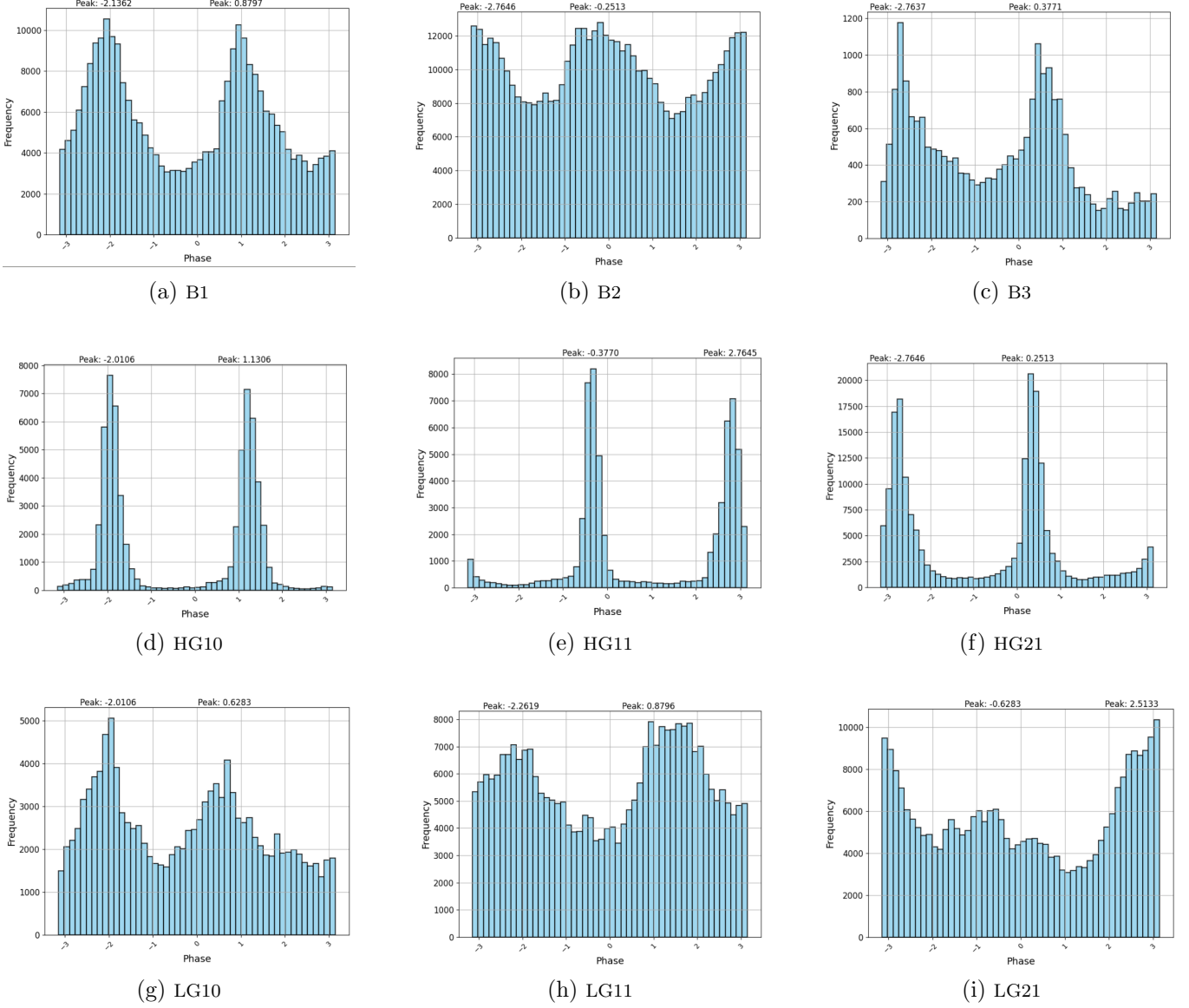


FIG. 12: Histogram of experimental phase diagram.

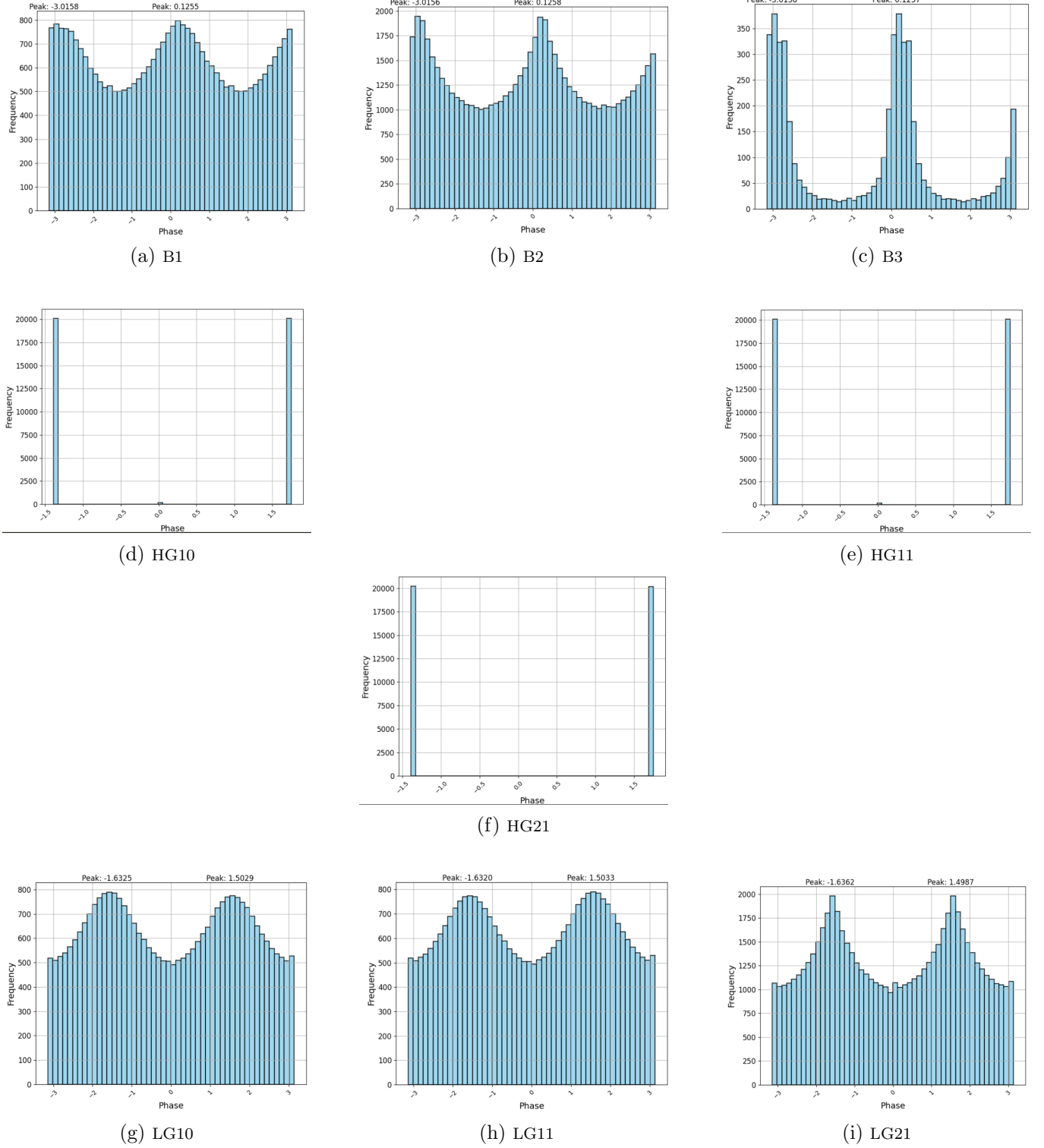


FIG. 13: Histogram of predicted phase diagram